

Article

S, Se-Codoped Dual Carbon Coating and Se Substitution in Co-Alkoxide-Derived CoS₂ Through SeS₂ Triggered Selenization for High-Performance Sodium-Ion Batteries

Kaiqin Li [†], Yuqi Kang [†], Chengjiang Deng [†], Yanfeng Wang, Haocun Ba, Qi An, Xiaoyan Han ^{*} and Shaozhuang Huang ^{*}

Key Laboratory of Catalysis and Energy Materials Chemistry of Ministry of Education & Hubei Key Laboratory of Catalysis and Materials Science, South-Central Minzu University, Wuhan 430074, China

* Correspondence: xyhan@scuec.edu.cn (X.H.); husz001@scuec.edu.cn (S.H.)

[†] These authors contributed equally to this work.

Abstract: The development of metal sulfides as anodes for sodium-ion batteries (SIBs) is significantly obstructed by the slow kinetics of the electrochemical reactions and the substantial volume changes on the cycling. Herein, we introduce a selenium-substituted cobalt disulfide embedded within a dual carbon-graphene framework (Se-CoS₂/C@rGO) for high-performance SIBs. The Se-CoS₂/C@rGO was prepared via a synchronous sulfurization/selenization strategy using Co-alkoxide as the precursor and SeS₂ as the source of selenium and sulfur, during which the EG anions are converted *in situ* to a S, Se codoped carbon scaffold. The dual carbon-graphene matrix not only improves the electronic conductivity but also stabilizes the electrode material effectively. In addition, the Se substitution within the CoS₂ lattice further improves the electrical conductivity and promotes the Na⁺ reaction kinetics. The enhanced intrinsic electronic/ionic conductivity and reinforced structural stability endow the Se-CoS₂/C@rGO anode with a high reversible capacity (558.2 mAh g⁻¹ at 0.2 A g⁻¹), superior rate performance (351 mAh g⁻¹ at 20 A g⁻¹), and long cycle life (93.5% capacity retention after 2100 cycles at 1 A g⁻¹). This work provides new insights into the development of stable and reversible anode materials through Se substitution and dual carbon encapsulation.



Academic Editor: Diana Golodnitsky

Received: 3 December 2024

Revised: 27 December 2024

Accepted: 10 January 2025

Published: 15 January 2025

Citation: Li, K.; Kang, Y.; Deng, C.; Wang, Y.; Ba, H.; An, Q.; Han, X.; Huang, S. S, Se-Codoped Dual Carbon Coating and Se Substitution in Co-Alkoxide-Derived CoS₂ Through SeS₂ Triggered Selenization for High-Performance Sodium-Ion Batteries. *Batteries* **2025**, *11*, 28. <https://doi.org/10.3390/batteries11010028>

Copyright: © 2025 by the authors. Licensee MDPI, Basel, Switzerland. This article is an open access article distributed under the terms and conditions of the Creative Commons Attribution (CC BY) license (<https://creativecommons.org/licenses/by/4.0/>).

1. Introduction

Currently, the excessive consumption and uneven distribution of lithium resources result in the high production costs of commercial lithium-ion batteries (LIBs) [1–3]. The development of affordable and sustainable rechargeable batteries has thus become an urgent topic recently [4]. Sodium-ion batteries (SIBs), with their low cost, abundant resources, and similar working principle to LIBs, are increasingly being recognized as a promising alternative for large-scale energy storage [5–7]. Furthermore, unlike LIBs which have a relatively low energy density [8], metal lithium batteries that form lithium dendrites during the charging process [9], and solid-state batteries that exhibit slow kinetics [10], sodium-ion batteries offer distinct advantages in energy density, safety, and kinetics, thereby demonstrating significant development potential. However, the larger radius of Na⁺ (1.02 Å) compared to Li⁺ (0.76 Å) leads to sluggish Na⁺ diffusion kinetics, significant volume changes, and

potential structural damage to electrode materials during the sodiation/desodiation processes, resulting in rapid capacity degradation [11]. Therefore, exploring suitable electrode materials that offer high cyclic stability and specific capacity become a primary challenge in the research of SIBs [12,13].

Over the past decade, a variety of electrode materials have been developed, including transition metal oxides [14], sulfides [15], and phosphides [16]. Recently, transition metal sulfides (TMSs), such as FeS_2 [17], CoS_2 [12], and MoS_2 [18], have been extensively investigated due to their high theoretical capacity and decent electrochemical activity. Moreover, metal–sulfur bonds in TMSs are more susceptible to breaking during the conversion reaction compared to oxides, which can potentially enhance the reaction kinetics [19,20]. Although cobalt compounds can cause certain harm to the environment, they have rather prominent functionality and are widely used in many fields such as catalysis, batteries and magnetic materials. Cobalt compounds possess a high theoretical sodium storage capacity, can undergo abundant redox reactions and have excellent electrochemical properties, making them an outstanding electrode material. In particular, cobalt disulfide (CoS_2), with large theoretical capacity (870 mAh g^{-1}) and moderate electronic conductivity, has emerged as a compelling candidate for sodium storage and has attracted considerable research interest [21]. However, CoS_2 -based anodes suffer from substantial volume changes and sluggish reaction kinetics during cycling, leading to electrode pulverization and poor cycling stability [12]. To overcome the issues of large volume variation and the sluggish reaction kinetics of CoS_2 , and bridge the gap between its theoretical and practical performance, various modification strategies have been proposed, primarily categorized into three groups: nanoscale design [22], conductive composite modification [23], and heteroatom doping [24]. While nanoscale design and conductive composite modification can improve ion/electron transfer efficiency, they may not effectively enhance the intrinsic electronic and ionic conductivity in the electrode materials [25]. Among the numerous carbonaceous materials used as substrates, graphene has been widely studied due to its large theoretical specific surface area, outstanding thermal stability, superior electronic conductivity, and remarkable structural flexibility. Moreover, the flexible and conductive rGO nanosheets can effectively inhibit the electrode volume expansion during the charging/discharging process. Based on the features mentioned above, graphene can be used to improve the electrochemical performance of electrodes.

Heteroatom doping has been widely applied to carbonaceous materials and could effectively improve the defects, porosity, interlayer spacing, and conductivity [26]. In particular, selenium (Se) doping/substitution has shown great efficacy in improving the rate capability of carbonaceous materials, attributed to the increased number of Na-ion adsorption sites [27]. For TMSs, the substitution of Se for S could narrow the band gaps and improve the electronic conductivity of TMSs since the valence electrons of the Se atom experience less constraint from the nuclear charge than those of the S atom due to the enhanced shielding effect [28]. Moreover, the bond energy of metal–Se is weaker than that of metal–S bond, giving rise to enhanced redox kinetics during the conversion reactions. For example, Huang et al. reported on the few-layered MoS₂ nanoribbons for SIBs, which deliver better sodium storage performance than the MoS_2 [27]. Even with these emerging reports, some inadequacies still remain based on this interesting system: (1) In the majority of instances, the large volume change on the cycling makes it difficult for TMSs to achieve a long cycle life (>1500 cycles) with high capacity retention (>90%). (2) The Se substituted TMSs are mainly obtained by using either Se in hydrazine hydrate or a S/Se mixture as the selenium source, which may cause environmental issues or induce an inaccurate Se substitution ratio due to the distinct melting and boiling points of sulfur and selenium [27].

(3) The external single carbon coating strategy cannot well encapsulate the active materials, leading to electrode pulverization upon long-term cycling [29].

Herein, we develop a novel sulfurization/selenization process to conduct the Se substitution in CoS_2 , where the Co-alkoxide was used as the precursor and SeS_2 served as the Se and S source. The SeS_2 serves as a single source to conduct the Se substitution, which can reduce the uncontrollability of the sulfurization/selenization process in comparison to the general method using the sulfur/selenium powder source. Moreover, the alkoxide anions are transformed in situ to carbon scaffold in the sulfurization/selenization process, during which the evaporation of SeS_2 also leads to S, Se codoping in the carbon matrix. The introduction of selenium ions (Se^{2-}) into CoS_2 significantly improves the Na^+ diffusion kinetics. Moreover, the reduced graphene oxide (rGO) encapsulation effectively improves the electronic conductivity and further stabilizes the CoS_2 . Thus, the obtained $\text{Se-CoS}_2/\text{C}@\text{rGO}$ delivers high specific capacity (558.2 mAh g^{-1} at 0.2 A g^{-1}), excellent rate capability (351.2 mAh g^{-1} at 20 A g^{-1}), and a superior cycle lifespan (93.5% capacity retention after 2100 cycles).

2. Experimental Section

Synthesis of Co-EG@rGO: The synthesis of Co-EG@rGO is according our previous work [30]: firstly, 45 mg of monolayer graphene oxide (Suzhou Technology Co., Suzhou, China) was dispersed in 40 mL ethylene glycol (EG) and kept under ultrasonication for 30 min. Then, 498 mg of $(\text{Co}(\text{CHCOO})_2 \cdot 4\text{H}_2\text{O}$ and 100 mg of LiOH were dissolved in 40 mL EG to obtain a pink solution, which was dropwise added to the above GO suspension under vigorous stirring, and then continuously stirred for 30 min. Subsequently, the suspension was transferred to a 250 mL round-bottom flask and heated at 165 °C for 3 h in Ar. Then the precipitation was washed with absolute ethanol several times and finally dried under vacuum at 60 °C for 6 h to obtain the Co-EG@rGO.

Synthesis of Se-CoS₂/C@rGO: The $\text{Se-CoS}_2/\text{C}@\text{rGO}$ was prepared through a synchronous selenization/sulfurization method. Specifically, the Co-EG@rGO precursor and SeS_2 were each placed in the downstream and upstream of a quartz boat. Then, the selenization/sulfurization was conducted under Ar atmosphere at 500 °C for 2 h at a temperature ramping of 2 °C min⁻¹. The atomic ratios of S: Se were set as two groups: pure S and SeS_2 . The mass ratio of S/ SeS_2 to Co-EG@rGO was kept at 5:1. The obtained samples are $\text{CoS}_2/\text{C}@\text{rGO}$ and $\text{Se-CoS}_2/\text{C}@\text{rGO}$, respectively.

Material characterization: The crystal structures of samples were tested by the X-ray diffractometer (XRD, D8 ADVANCE, Shenzhen, China) with Cu K α radiation ($\lambda = 1.541 \text{ \AA}$), where the sweep speed was 0.3 s/step, the step length was 0.05 degrees/step, and the scanning range was 5~80 degrees. Raman spectra were obtained using a Raman microscope (DXR2 XI, Waltham, MA, USA) with a laser wavelength of 532 nm. The chemical states of all the samples were analyzed by X-ray photoelectron spectroscopy (XPS, EscalabXi+, Reading, UK). The morphology and structure were investigated using field emission scanning electron microscopy (FESEM, SU8010, Zeiss, Germany) and transmission electron microscopy (TEM, FEI TALOS F200X, Tokyo, Japan). Energy-dispersive X-ray spectroscopy analysis was carried out in the TEM.

Electrochemical tests: The above materials as working electrode and sodium metal foil as counter electrode were assembled in an Ar-filled glove box ($\text{H}_2\text{O} < 0.01 \text{ ppm}$, $\text{O}_2 < 0.01 \text{ ppm}$). The working electrodes were made by grinding the active material, polyvinylidene fluoride (PVDF) and Ketjen black, which were dispersed in NMP solvent at a mass ratio of 8:1:1, and then coated on the copper foil and dried in a vacuum oven at 60 °C for 12 h. The mass loading of the electrode was 0.8–1.2 mg cm^{-2} . A measured sample of 1 M NaPF₆ (Sigma, Kawasaki-shi, Japan, 98%) in DME (Sigma) was used as electrolyte

and Whatman GF/D glass fiber was adopted as the separator. The galvanostatic charge-discharge and galvanostatic intermittent titration technique (GITT) tests were performed by a NEWARE battery testing system with potential of 0.01–2.5 V. The GITT was carried out with a current pulse of 0.2 A g^{-1} for 900 s and relaxation for 900 s. CV curves were measured at various scan rates from 0.1 to 1.0 mV s^{-1} on an IVIUM electrochemical workstation, and EIS measurements were tested in the frequency range of 100 kHz–0.01 Hz on the same electrochemical workstation.

3. Results and Discussion

The Se-CoS₂/C@rGO was prepared by sulfurization/selenization of the Co-alkoxide@rGO (Co-EG@rGO, EG represents ethylene glycol), as schematically shown in Figure 1. Firstly, Co-EG@rGO was synthesized through the reactions between ethylene glycol solvent and Co²⁺ as per our previous work [30] (Figure S1). During the synthesis, the Co²⁺ ions were firstly adsorbed on the negatively charged graphene oxide; at the same time, EG⁻ or EG²⁻ ions were generated with the assistance of LiOH following the dissociation reactions: $\text{C}_2\text{H}_4(\text{OH})_2 \leftrightarrow [\text{(C}_2\text{H}_4)\text{O}_2\text{H}]^- + \text{H}^+$; $[\text{(C}_2\text{H}_4)\text{O}_2\text{H}]^- \leftrightarrow [\text{(C}_2\text{H}_4)\text{O}_2]^{2-} + \text{H}^+$. After that, the Co-EG was acquired through the coordination reaction between EG⁻ or EG²⁻ dianion and Co²⁺, forming the $\text{Co}(\text{EG}^-)_x(\text{EG}^{2-})_y$ [30]. In the meantime, the graphene oxide was reduced to rGO by reductive EG solvent, forming the Co-EG/rGO composite. Finally, the Se substituted Se-CoS₂/C@rGO was obtained through a synchronous selenization/sulfurization of the Co-EG@rGO precursor by using the SeS₂ as the selenium/sulfur sources, where the Co-EG was converted to Se-CoS₂ and EG anions were transformed in situ into carbon scaffold [31]. The formation of carbon scaffold can be confirmed by the element maps of bare Se-CoS₂ (selenization/sulfurization of bare Co-EG) (Figure S2), where the obvious carbon signal refers to the carbon scaffold. Also, the S: Se atomic ratio was estimated to be 2.1:1 based on the energy dispersive X-ray spectroscopy (EDS), close to the atomic ratio of SeS₂. The reaction between SeS₂ and Co-EG should be ascribed to the following reaction processes:

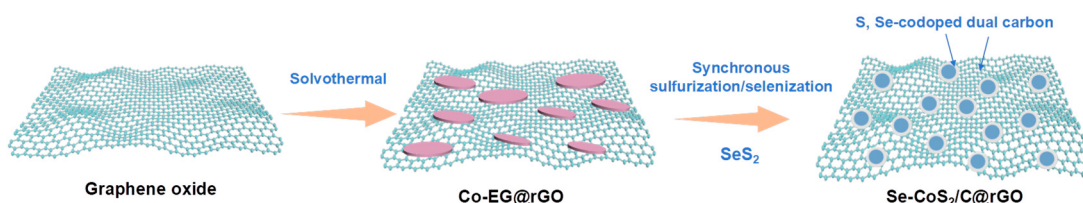
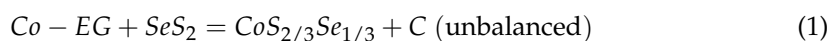


Figure 1. Schematic representation of the synthesis process for Se-CoS₂/C@rGO composites.

As a comparison, the CoS₂/C was prepared using the S as the sulfurization agent, as described below:



The crystal structure of the prepared CoS₂/C@rGO and Se-CoS₂/C@rGO samples was analyzed using X-ray diffraction (XRD). As shown in Figure 2a,b, all the diffraction peaks of CoS₂/C@rGO can be indexed to the cubic CoS₂ with the *P*a-3 space group (JCPDS No. 04-004-4839) [32], indicating the high purity and good crystallinity of the CoS₂ nanoparticles. In contrast, after Se substitution, the diffraction peaks of Se-CoS₂/C@rGO exhibit a significant shift towards lower angles due to the unit cell expansion, confirming the successful Se replacement of S at the atomic level. The cell volume expansion upon selenium substitution could significantly relieve the crystal strain and enhance the Na⁺ diffusion kinetics.

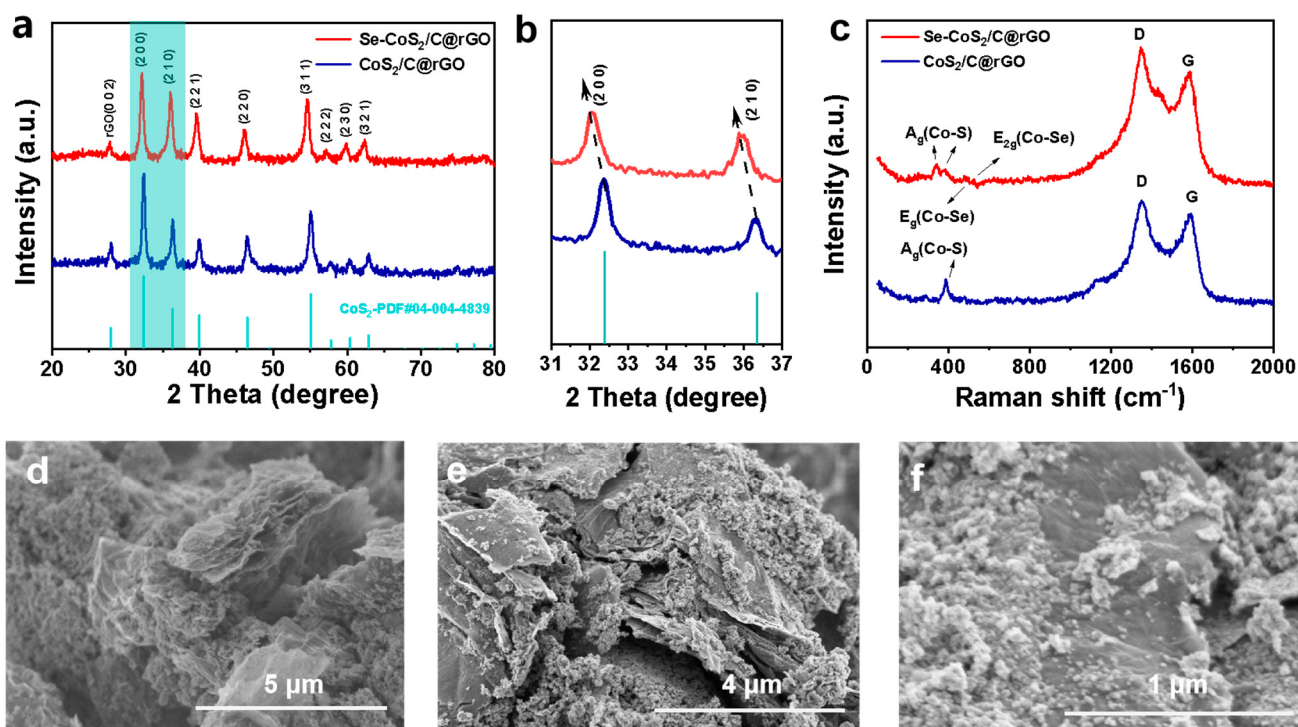


Figure 2. (a,b) XRD patterns of $\text{CoS}_2/\text{C}@\text{rGO}$ and $\text{Se}-\text{CoS}_2/\text{C}@\text{rGO}$, (c) Raman spectra of $\text{CoS}_2/\text{C}@\text{rGO}$ and $\text{Se}-\text{CoS}_2/\text{C}@\text{rGO}$. (d) SEM images of $\text{CoS}_2/\text{C}@\text{rGO}$ and (e,f) $\text{Se}-\text{CoS}_2/\text{C}@\text{rGO}$.

The structural transformation of the samples under selenium substitution was further investigated by Raman spectroscopy. As presented in Figure 2c, the two distinct Raman peaks at 1352 and 1588 cm^{-1} correspond to the D (indicative of disordered or defective structures) and G bands (representative of graphitic structures) of the carbon matrix (C and rGO), respectively [33]. Notably, the I_D/I_G ratio of $\text{Se}-\text{CoS}_2/\text{C}@\text{rGO}$ (1.24) is much higher than that of $\text{CoS}_2/\text{C}@\text{rGO}$ (1.06), suggesting more abundant defects in the carbon matrix due to the S and Se heteroatom doping, which is believed to tailor the electronic structure of carbon framework to improve the sodium storage capability [34]. As for $\text{CoS}_2/\text{C}@\text{rGO}$, the peak at 388 cm^{-1} is ascribed to the A_g mode of CoS_2 [35,36]. After Se substitution, the A_g mode of CoS_2 splits into two peaks around 338 and 383 cm^{-1} , which may stem from the atomic rearrangement and structural strain because of the Se substitution [37]. Moreover, two new peaks at 475 and 524 cm^{-1} appear in the $\text{Se}-\text{CoS}_2/\text{C}@\text{rGO}$, which are associated with the E_g and E_{2g} modes of Co-Se [38].

The morphology of the $\text{CoS}_2/\text{C}@\text{rGO}$ and $\text{Se}-\text{CoS}_2/\text{C}@\text{rGO}$ samples was examined using scanning electron microscopy (SEM). Figure 2d depicts the SEM image of $\text{CoS}_2/\text{C}@\text{rGO}$, which consists of nanoparticles ($50\text{--}100 \text{ nm}$) anchored to the graphene nanosheets. This nanoscale size not only reduces the Na^+ diffusion distance but also creates plentiful active sites which productively enhance the charge-transfer dynamics and facilitate interfacial charge storage [39,40]. After Se substitution, the morphology of the $\text{Se}-\text{CoS}_2/\text{C}@\text{rGO}$ sample remains nearly unchanged, suggesting a robust chemical interaction between CoS_2 nanoparticles and rGO during the synchronous sulfurization/selenization process (Figure 2e,f).

X-ray photoelectron spectroscopy (XPS) was employed to analyze the elements and valence states of the $\text{CoS}_2/\text{C}@\text{rGO}$ and $\text{Se}-\text{CoS}_2/\text{C}@\text{rGO}$ samples. As shown in Figure S3, the survey XPS spectrum of the $\text{Se}-\text{CoS}_2/\text{C}@\text{rGO}$ confirms the presence of Co, Se, S, and C elements in the composite. In the high-resolution Co 2p XPS spectrum of $\text{CoS}_2/\text{C}@\text{rGO}$ (Figure 3a), the main peaks at 779.1 and 794.2 eV correspond to the spin-orbit characteristic peaks of $\text{Co } 2p_{3/2}$ and $\text{Co } 2p_{1/2}$ in CoS_2 , respectively [33]. The peaks at 782.1 and 798.3 eV

are associated with the surface CoO_x species. Additional peaks at 785.8 and 803.7 eV are attributed to the satellite peaks of Co 2p, associated with oscillatory excitation of high-spin Co^{2+} ions, demonstrating the presence of cobalt (II) [41,42]. After Se substitution, the Co 2p_{3/2} peak shifts to a lower binding energy (from 779.1 eV to 778.8 eV), indicative of Co atoms bonding with the less electronegative Se atoms. This shift suggests that the selenium substitution can modulate the d-band electronic structure of the Co atoms. In the high-resolution S 2p spectrum of $\text{CoS}_2/\text{C@rGO}$ (Figure 3b), the spin-orbit doublets at 163.1 and 164.3 eV correspond to the S 2p_{3/2} and S 2p_{1/2}, respectively [26]. Furthermore, the broad peaks at 169.2 and 170.3 eV are assigned to the surface sulfur oxide species (SO_x). With Se incorporation, the S 2p peaks of $\text{Se-CoS}_2/\text{C@rGO}$ shift to lower binding energies, indicating successful Se doping in CoS_2 crystals that enriches the electron cloud around the S atoms [43]. Additionally, the doublet peaks at 161.1 and 166.0 eV correspond to the Se 3p_{3/2} and Se 3p_{1/2}, respectively, confirming successful Se doping. The Se incorporation was further verified by the Se 3d spectrum, where the peaks 55.4 and 56.3 eV are assigned to the Se 3d_{5/2} and Se 3d_{3/2}, respectively (Figure 3c). The C 1s spectrum of $\text{Se-CoS}_2/\text{C@rGO}$ (Figure 3d) can be deconvoluted into four peaks at 284.8, 285.4, 285.9, and 288.8 eV, representing C-C, Se-C, S-C, and C=O bonds, respectively [44,45]. The C 1s spectrum indicates the formation of a S, Se-codoped carbon matrix from the sulfurization/selenization process.

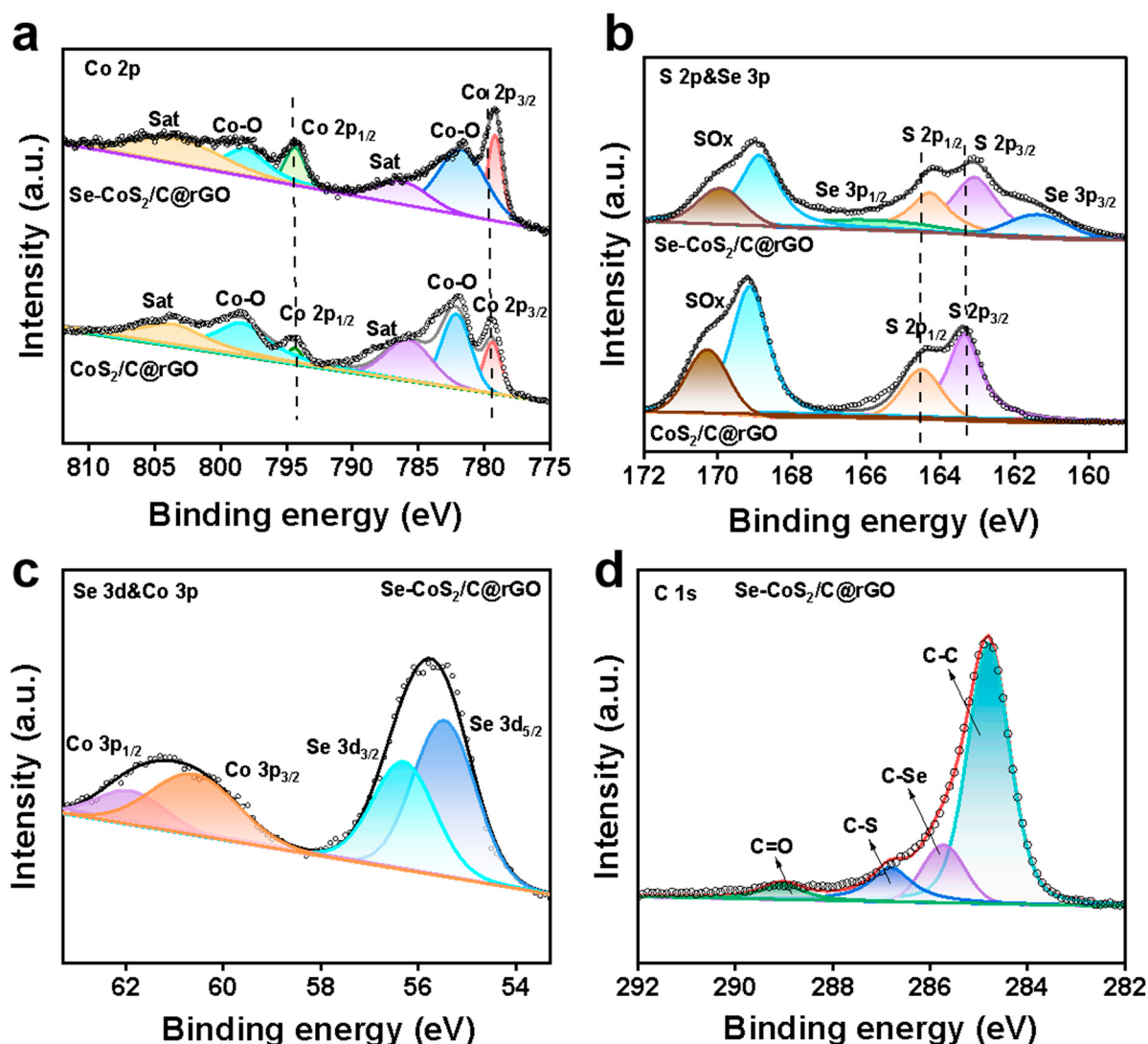


Figure 3. High-resolution XPS spectra of Co 2p (a), S 2p and Se 3p (b), Se 3d and Co 3p (c) and C 1s (d).

The microstructure of the Se-CoS₂/C@rGO sample was further examined using transmission electron microscopy (TEM). It was revealed that the Se-CoS₂/C@rGO consists of nanoparticles uniformly dispersed on the graphene nanosheet. This structure can effectively suppress the nanoparticle agglomeration and buffer volume expansion on cycling. The high-resolution TEM (HRTEM) image (Figure 4b) displays distinct lattice fringes with a measurable lattice spacing of 2.78 Å, corresponding to the (200) plane of the Se-CoS₂. This lattice spacing is slightly larger than that of the (200) plane of standard pyrite CoS₂ ($D_{200} = 2.76$ Å, JCPDS No. 04-004-4839) [32], suggesting a lattice expansion due to Se substitution in CoS₂, which is in good agreement with the XRD result. This lattice expansion is attributed to the larger ionic radius of Se²⁻ (1.98 Å) compared to S²⁻ (1.84 Å). The corresponding selected area electron diffraction (SAED) pattern displays a series of different concentric diffraction rings (Figure 4c), demonstrating the polycrystalline nature of Se-CoS₂/C@rGO. The scanning TEM energy dispersive spectroscopy (STEM-EDS) elemental mapping images of Se-CoS₂/C@rGO distinctly reveal the coexistence and uniform distribution of Co, S, Se and C elements across the sample, displaying the uniform and successful Se substitution in CoS₂ (Figure 4d). These results are in good accord with the XRD and XPS analysis.

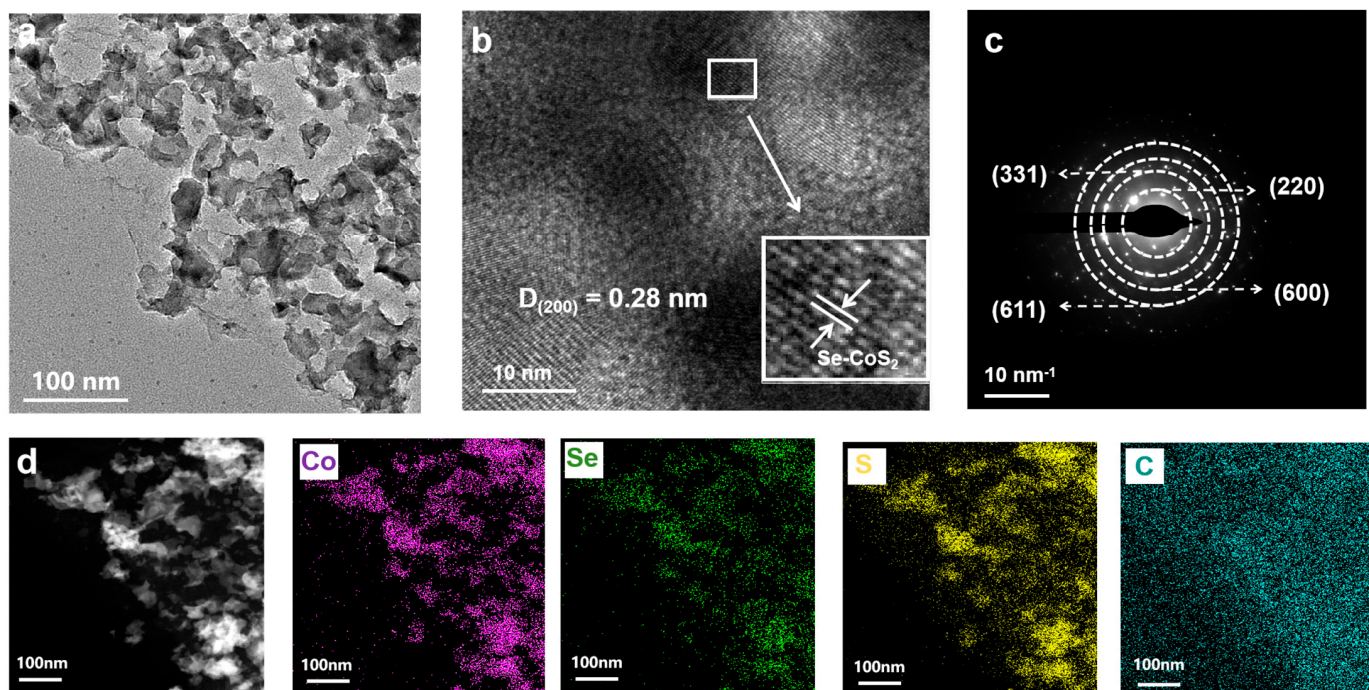


Figure 4. (a) TEM image of Se-CoS₂/C@rGO, (b) HRTEM image of Se-CoS₂/C@rGO, (c) SAED pattern of Se-CoS₂/C@rGO, (d) STEM-EDS elemental mapping of Se-CoS₂/C@rGO.

To investigate the discharge-charge behavior of the Se-CoS₂/C@rGO electrode, cyclic voltammetry (CV) testing was conducted from 0.01 V to 2.5 V at a scan rate of 0.1 mV s⁻¹ (Figure 5a). During the first cathodic scan, the peaks at 1.20 V and 0.79 V can be attributed to the initial Na⁺ insertion reaction and the formation of a solid electrolyte interphase (SEI) layer, respectively [28]. The strong peak at 0.63 V can be attributed to the conversion of Na⁺ intercalated Se-CoS₂ to Co and Na₂S/Na₂Se [28]. During the first anodic scan, the three oxidation peaks at 1.78 V, 1.90 V, and 2.01 V correspond to the multistep desodiation of Na₂S/Na₂Se back to Se-CoS₂ [35]. From the second scan, the initial cathodic peak shifts to 1.45 V, which is a result of the electrochemical activation process and structural reorganization of the electrode [26,28]. Then the sodium storage performance of the CoS₂/C@rGO and Se-CoS₂/C@rGO was evaluated and compared. Figure 5b illustrates the galvan-

static charge/discharge profiles within the potential range of 0.01 to 2.5 V at a current density of 0.2 A g^{-1} . The Se-CoS₂/C@rGO electrode delivers a higher specific capacity than the CoS₂/C@rGO, with initial discharge and charge specific capacities of 629.7 and 583.4 mAh g^{-1} , respectively, corresponding to a high initial Coulombic efficiency of 92.6%. Moreover, the Se-CoS₂/C@rGO electrode displays much smaller voltage hysteresis than the CoS₂/C@rGO, demonstrating better conversion reaction kinetics. Subsequent cycles of Se-CoS₂/C@rGO demonstrate a Coulomb efficiency approaching 98.3%, highlighting the excellent electrochemical reversibility of the Se-CoS₂/C@rGO composite (Figure 5c). After 40 cycles, the capacity of Se-CoS₂/C@rGO remains a high value of 528.5 mAh g^{-1} , higher than the CoS₂/C@rGO (421.7 mAh g^{-1}). The better cycling stability of the Se-CoS₂/C@rGO underscores the beneficial impact of Se substitution on enhancing the structural integrity throughout the cycling process. This result also indicates that the cell volume expansion (via Se incorporation) of the Se-CoS₂ could effectively relieve the crystal strain generated by Na⁺ intercalation/deintercalation.

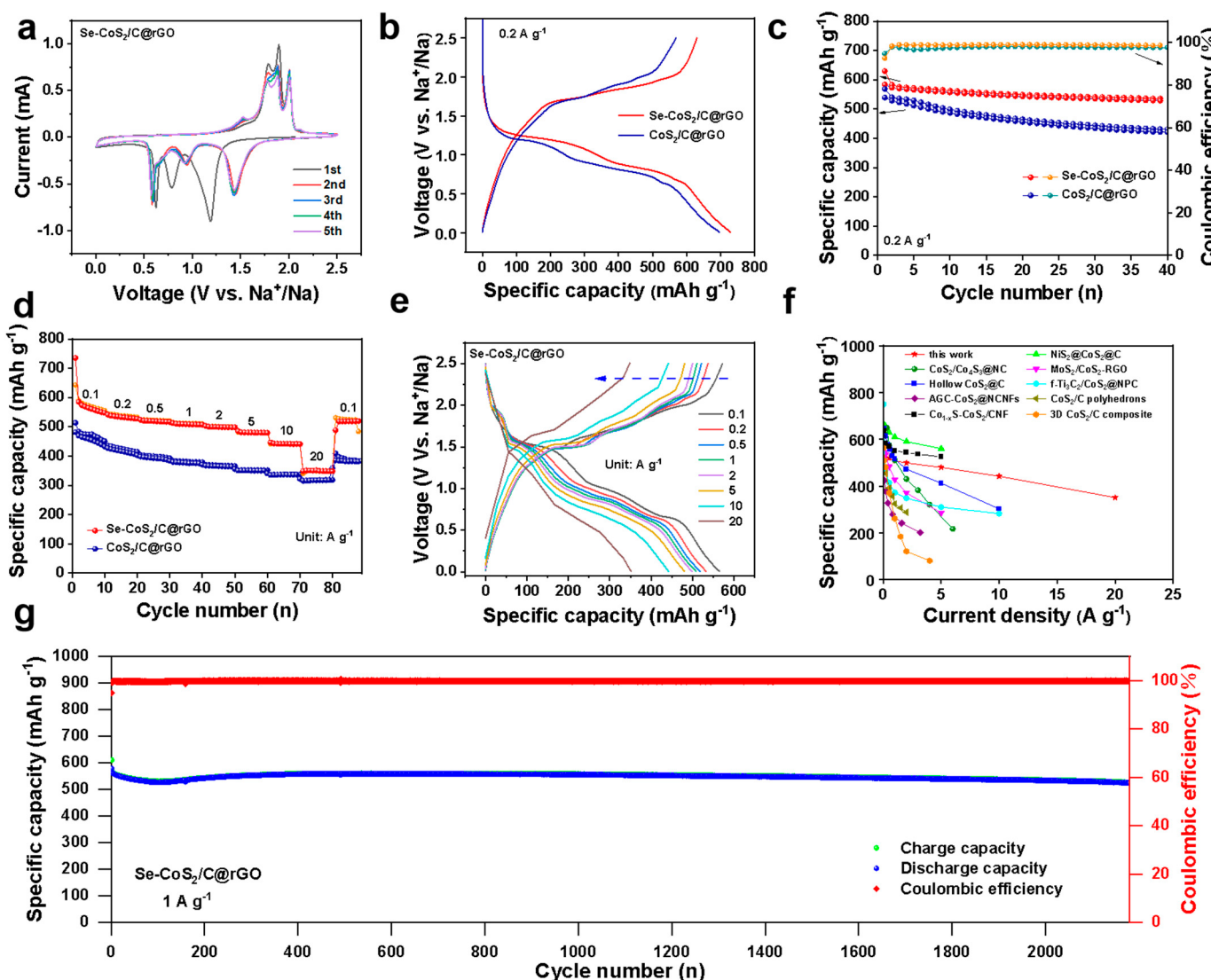


Figure 5. Electrochemical performance of CoS₂/C@rGO and Se-CoS₂/C@rGO. (a) CV curve from 0.01 V to 2.5 V vs. Na⁺/Na at a scan rate of 0.1 mV s^{-1} , (b) discharge and charge profiles of Se-CoS₂/C@rGO electrode at the first cycle, (c) cycling performance at 0.2 A g^{-1} , (d) rate capabilities at various current densities, (e) discharge and charge profiles of Se-CoS₂/C@rGO electrode at different current densities, (f) rate comparison of CoS₂-based works. (g) Long-term cycling performance at 1 A g^{-1} .

Figure 5d,e display the rate capability of the $\text{CoS}_2/\text{C@rGO}$ and $\text{Se-CoS}_2/\text{C@rGO}$. It is evident that the $\text{Se-CoS}_2/\text{C@rGO}$ composite exhibits superior rate capability compared to the $\text{CoS}_2/\text{C@rGO}$ electrode, showing specific capacities of 560, 533, 519, 508, 499, 480, 442, and 351 mAh g^{-1} at current densities of 0.1, 0.2, 0.5, 1, 2, 5, 10, and 20 A g^{-1} , respectively. When the current density turns back to 0.1 A g^{-1} , the specific capacity can recover to 519 mAh g^{-1} , indicating the good reversibility. The excellent rate capability of $\text{Se-CoS}_2/\text{C@rGO}$ is attributed to the synergistic effect of Se substitution and dual carbon matrix incorporation that facilitate fast electron/ Na^+ transportation. The outstanding rate capability of $\text{Se-CoS}_2/\text{C@rGO}$ is one of the best among all the CoS_2 -based materials for SIBs (Figure 5f) [46–54]. Then the long-term cycling performance of the $\text{Se-CoS}_2/\text{C@rGO}$ electrode was tested at a current density of 1 A g^{-1} . As depicted in Figure 5g, the $\text{Se-CoS}_2/\text{C@rGO}$ electrode exhibited a high specific capacity of 529.5 mAh g^{-1} after 2100 cycles, corresponding to an ultrahigh capacity retention of 93.5% (0.003% capacity decay per cycle). Compared with other CoS_2 materials, $\text{Se-CoS}_2/\text{C@rGO}$ materials possess higher specific capacity, better charge-discharge efficiency and longer cycle life [50–52].

To better understand the electrochemical reaction kinetics of the $\text{Se-CoS}_2/\text{C@rGO}$ electrode, a kinetic study of the CV curves was conducted at scan rates ranging from 0.2 to 1.0 mV s^{-1} (Figure 6a). As the scan rate increased, the redox peaks of $\text{Se-CoS}_2/\text{C@rGO}$ electrodes were well-maintained without significant peak shifts, indicating the high reversibility and low polarization of the electrodes. The relationship between peak current (i) and scan rate (v) can be described by the following equations [21,26]:

$$i = av^b \quad (3)$$

$$\log(i) = \log(a) + b\log(v) \quad (4)$$

Here, the b -value, which is the slope of the linearly fitted straight line between $\log(i)$ and $\log(v)$, plays a crucial role in determining the kinetics of the sodium storage reaction of the material. As the b -value approaches 0.5, sodium storage is dominated by diffusive behavior, whereas a b -value close to 1 indicates that the electrochemical process is dominated by surface pseudocapacitive processes [26,43]. Figure 6b shows the plots of $\log(i)$ versus $\log(v)$ at oxidation and reduction peaks 1 to 4, with b -values of 0.71, 0.67, 0.78 and 0.79, respectively. This suggests that the redox reactions at peaks 1 to 4 exhibit a combination of both diffusive and pseudocapacitive behaviors. The pseudocapacitance contribution at different scan rates can be calculated using Equation 5:

$$i(V) = k_1v + k_2v^{1/2} \quad (5)$$

Here, $i(V)$ is the total current response at a given potential V , and k_1v represents the current from capacitive behavior [55]. Based on the above equation, the pseudocapacitance contributions at 0.2, 0.4, 0.6, 0.8, and 1.0 mV s^{-1} are calculated to be approximately 89.3%, 94.1%, 96.1%, 97.4%, and 98.0%, respectively (Figure 6c). As shown in Figure 6d, the pseudocapacitance contribution at a scan rate of 1.0 mV s^{-1} reaches as high as 98.0%, suggesting that the charge storage at high rate is dominated by the surface pseudocapacitive process. Such a high capacitance contribution facilitates the ultra-fast Na^+ migration, contributing to the excellent rate performance of the $\text{Se-CoS}_2/\text{C@rGO}$ electrode.

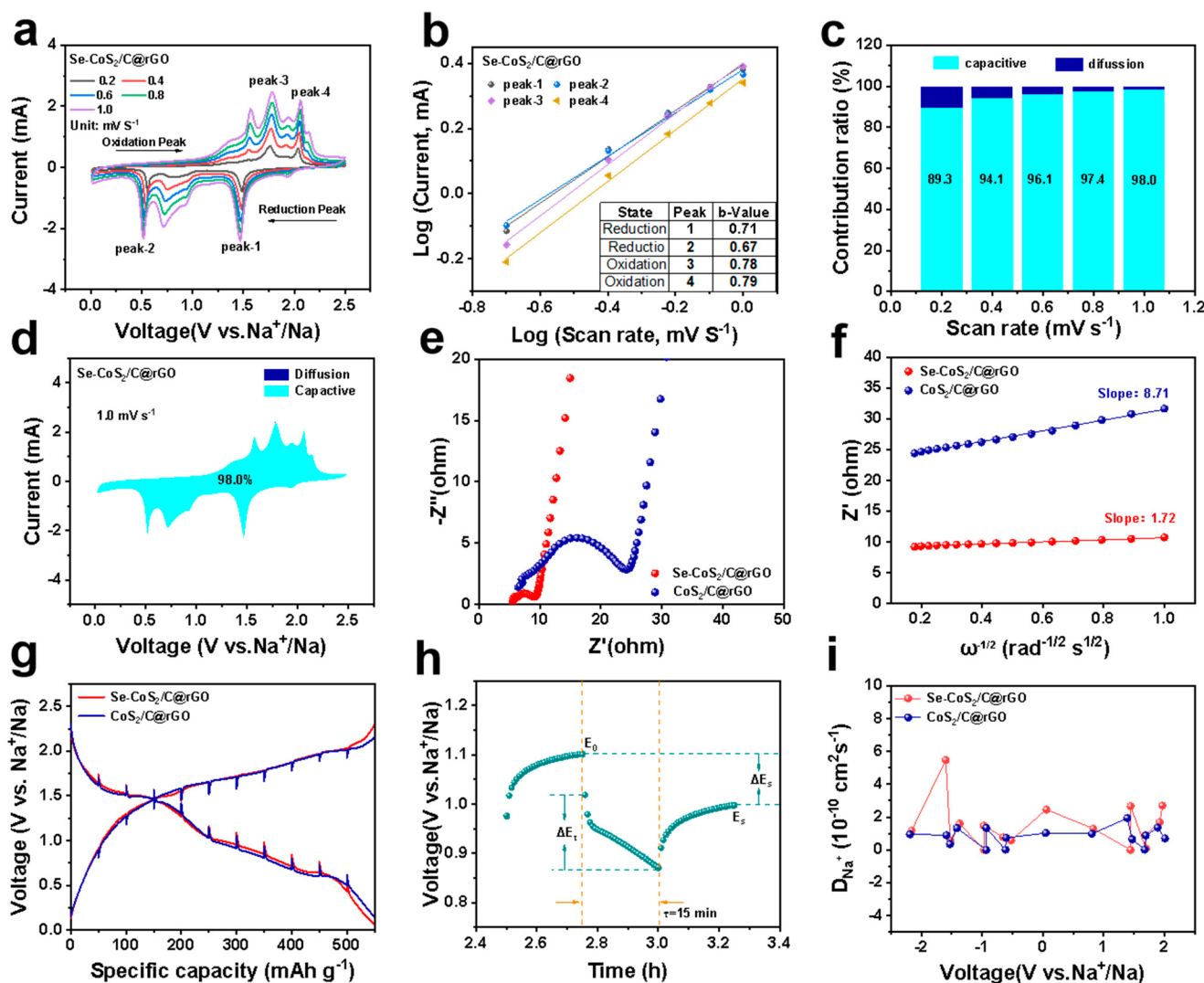


Figure 6. (a) Scan-rate-dependent CV curves, (b) the plots of $\log i$ and $\log v$ at each redox peak, (c) the normalized percentage of capacitive contributions at distinct scan rates, (d) capacitive charge contribution at 1.0 mV s^{-1} , (e) the initial EIS patterns, (f) relationship of Z' versus $\omega^{-1/2}$, (g) GITT profiles at pulse current of 0.2 A g^{-1} , (h) voltage (V) versus time (t) profiles of the Se-CoS₂/C@rGO electrode for a single GITT during the discharge process, (i) the corresponding D_{Na^+} values.

To further investigate the kinetic behavior of the material, we analyzed the initial electrochemical impedance spectra (EIS) (Figure 6e). The semicircular feature at high frequencies indicates the charge transfer impedance at the electrode/electrolyte interface [56]. It is evident that the charge transfer resistance of the Se-CoS₂/C@rGO electrode is notably lower than that of the CoS₂/C@rGO electrode, underscoring that Se substitution for S significantly enhances the electrical conductivity. Furthermore, the Na⁺-diffusion coefficient (D_{Na^+}) for both electrodes can be determined from the linear approximation of the real impedance Z' versus $\omega^{-1/2}$ and the corresponding equation: [27,57]

$$D = \frac{R^2 T^2}{2A^2 n^4 F^4 C^2 \sigma_w^2}. \quad (6)$$

where R, T, A, n, F and C represent gas constant, absolute temperature, area of electrode surface, the number of electrons, the Faraday constant and concentration of Na⁺, respectively. The σ_w stands for Warburg impedance coefficient in the low-frequency region, which can be obtained by the following equation:

$$Z' = R_S + R_{ct} + \sigma_w \omega^{-1/2} \quad (7)$$

By fitting Z' versus $\omega^{-1/2}$, the Se-CoS₂/C@rGO electrode exhibits a lower Warburg impedance coefficient (σ_w) than the CoS₂/C@rGO electrode (Figure 6f), suggesting enhanced Na⁺-diffusion kinetics. These findings align with the observed rate performance results. To gain a deeper understanding of the reasons for the significantly improved sodium storage performance of the Se-CoS₂/C@rGO electrodes, we performed the galvanostatic intermittent titration technique (GITT) curve tests on both electrodes at a current density of 0.2 A g⁻¹ (Figure 6g). The specific details of the GITT testing setup are provided in Figure 6h and are further elaborated in the Experimental Section. The Na⁺ apparent diffusion coefficients were calculated using the following formula [58]:

$$D_{Na^+} = \frac{4}{\pi \tau} \left(\frac{m_B V_M}{M_B S} \right)^2 \left(\frac{\Delta E_S}{\Delta E_\tau} \right)^2 \quad (8)$$

where τ represents the current pulse time (s), m_B is the mass of the active material, M_B denotes the molar mass, V_M is the molar volume, and S stands for the electrode area. The outcomes (Figure 6i) reveal that the diffusion coefficient of Se-CoS₂/C@rGO surpasses that of CoS₂/C@rGO, thereby reaffirming that the incorporation of Se enhances the diffusion kinetics of Na⁺.

4. Conclusions

We successfully prepared the Se-substituted CoS₂ embedded in carbon-graphene dual framework via the synchronous sulfurization/selenization strategy using the SeS₂ as the selenium/sulfur source. The rationally designed Se-CoS₂/C@rGO anode delivers a high initial Coulombic efficiency of 92.6%, high reversible capacity of 558.2 mAh g⁻¹ at 0.2 A g⁻¹, excellent rate performance of 351 mAh g⁻¹ at 20 A g⁻¹, and extended cycle life with a high capacity retention of 93.5% over 2100 cycles. The comprehensive performance and kinetic analysis highlight the substantial benefits of Se substitution and dual carbon encapsulation in conquering the limitations of traditional anode materials. This innovative structure not only improves the electrical conductivity and buffers the volume expansion but also sets new standards for energy density and capacity retention in SIBs. The development of Se-CoS₂/C@rGO is a significant step toward making SIBs commercially viable, providing a foundation for future advancements in sustainable energy storage technologies.

Supplementary Materials: The following supporting information can be downloaded at: <https://www.mdpi.com/article/10.3390/batteries11010028/s1>.

Author Contributions: Conceptualization, X.H. and S.H.; methodology, C.D.; software, Y.W.; validation, X.H., S.H. and K.L.; formal analysis, Q.A.; investigation, K.L., Y.W. and Y.K.; resources, S.H.; data curation, H.B.; writing—original draft preparation, K.L. and Y.K.; writing—review and editing, X.H. and K.L.; visualization, Q.A.; supervision, S.H.; project administration, X.H. and S.H.; funding acquisition, S.H. All authors have read and agreed to the published version of the manuscript.

Funding: This research was funded by the National Natural Science Foundation of China (Grant Number: 22109183), and “the Fundamental Research Funds for the Central Universities”, South-Central MinZu University (Grant Number: CZZ23002). And The APC was funded by 22109183.

Data Availability Statement: The raw data supporting the conclusions of this article will be made available by the authors on request.

Acknowledgments: This work was supported by the National Natural Science Foundation of China (22109183), and “the Fundamental Research Funds for the Central Universities”, South-Central MinZu University (Grant Number: CZZ23002).

Conflicts of Interest: The authors declare no conflict of interest.

References

- Yabuuchi, N.; Kubota, K.; Dahbi, M.; Komaba, S. Research development on sodium-ion batteries. *Chem. Rev.* **2014**, *114*, 11636–11682. [[CrossRef](#)] [[PubMed](#)]
- Hwang, J.-Y.; Myung, S.-T.; Sun, Y.-K. Sodium-ion batteries: Present and future. *Chem. Soc. Rev.* **2017**, *46*, 3529–3614. [[CrossRef](#)]
- Fan, E.; Li, L.; Wang, Z.; Lin, J.; Huang, Y.; Yao, Y.; Chen, R.; Wu, F. A Universal Molten Salt Method for Direct Upcycling of Spent Ni-rich Cathode towards Single-crystalline Li-rich Cathode. *Chem. Rev.* **2020**, *120*, 7020–7063. [[CrossRef](#)] [[PubMed](#)]
- Nayak, P.K.; Yang, L.; Brehm, W.; Adelhelm, P. Screening Heteroatom Configurations for Reversible Sloping Capacity Promises High-Power Na-Ion Batteries. *Angew. Chem. Int. Ed.* **2017**, *57*, 102–120. [[CrossRef](#)]
- Gao, Y.; Zhang, H.; Peng, J.; Li, L.; Xiao, Y.; Li, L.; Liu, Y.; Qiao, Y.; Chou, S.L. A 30-year overview of sodium-ion batteries. *Carbon Energy* **2024**, *6*, e464. [[CrossRef](#)]
- Rojo, T.; Hu, Y.-S.; Forsyth, M.; Li, X. Sodium-Ion Batteries. *Adv. Energy Mater.* **2018**, *8*, 1800880. [[CrossRef](#)]
- Zhao, Y.; Kang, Y.; Wozny, J.; Lu, J.; Du, H.; Li, C.; Li, T.; Kang, F.; Tavajohi, N.; Li, B. Recycling of sodium-ion batteries. *Nat. Rev. Mater.* **2023**, *8*, 623–634. [[CrossRef](#)]
- Zeng, C.; Zheng, R.; Fan, F.; Wang, X.; Tian, G.; Liu, S.; Liu, P.; Wang, C.; Wang, S.; Shu, C. Phase compatible surface engineering to boost the cycling stability of single-crystalline Ni-rich cathode for high energy density lithium-ion batteries. *Energy Storage Mater.* **2024**, *72*, 103788. [[CrossRef](#)]
- Yan, Y.; Shu, C.; Zheng, R.; Li, M.; Ran, Z.; He, M.; Hu, A.; Zeng, T.; Xu, H.; Zeng, Y. Modulating Sand's time by ion-transport-enhancement toward dendrite-free lithium metal anode. *Nano Res.* **2022**, *15*, 3150–3160. [[CrossRef](#)]
- Wang, S.; Wen, X.; Huang, Z.; Xu, H.; Fan, F.; Wang, X.; Tian, G.; Liu, S.; Liu, P.; Wang, C.; et al. High-Entropy Strategy Flattening Lithium Ion Migration Energy Landscape to Enhance the Conductivity of Garnet-Type Solid-State Electrolytes. *Adv. Funct. Mater.* **2024**, *34*, 2416389. [[CrossRef](#)]
- Wu, Y.; Shuang, W.; Wang, Y.; Chen, F.; Tang, S.; Wu, X.-L.; Bai, Z.; Yang, L.; Zhang, J. Enhanced Electrochemical Energy Storage of RGO@CoxSy through Nanostructural Modulation. *Electrochem. Energy Rev.* **2024**, *7*, 17.
- Li, T.; Wang, B.; Song, H.; Mei, P.; Hu, J.; Zhang, M.; Chen, G.; Yan, D.; Zhang, D.; Huang, S. Deciphering the Performance Enhancement, Cell Failure Mechanism, and Amelioration Strategy of Sodium Storage in Metal Chalcogenides-Based Anodes. *Adv. Mater.* **2024**, *36*, 2314271. [[CrossRef](#)] [[PubMed](#)]
- Qiao, S.; Zhou, Q.; Ma, M.; Liu, H.K.; Dou, S.X.; Chong, S. Interfacial electronic interaction enabling exposed Pt (110) facets with high specific activity in hydrogen evolution reaction. *ACS Nano* **2023**, *17*, 11220–11252. [[CrossRef](#)] [[PubMed](#)]
- Su, H.; Jaffer, S.; Yu, H. Understanding the mechanism of hydrogenated NiCo₂O₄ nanograss supported on Ni foam for enhanced-performance supercapacitors. *Energy Storage Mater.* **2016**, *5*, 116–131. [[CrossRef](#)]
- Yang, M.; Chang, X.; Wang, L.; Wang, X.; Gu, M.; Huang, H.; Tang, L.; Zhong, Y.; Xia, H. Interface Modulation of Metal Sulfide Anodes for Long-Cycle-Life Sodium-Ion Batteries. *Adv. Mater.* **2023**, *35*, 2208705. [[CrossRef](#)] [[PubMed](#)]
- Von Lim, Y.; Huang, S.; Zhang, Y.; Kong, D.; Wang, Y.; Guo, L.; Zhang, J.; Shi, Y.; Chen, T.P.; Ang, L.K.; et al. In-situ formation of nanostructured lithium manganese oxide cathode with enhanced electrochemical performance for lithium-ion batteries. *Energy Storage Mater.* **2018**, *15*, 98–107. [[CrossRef](#)]
- Wang, Q.H.; Guo, C.; Zhu, Y.X.; He, J.P.; Wang, H.Q. Reduced Graphene Oxide-Wrapped FeS₂ Composite as Anode for High-Performance Sodium-Ion Batteries. *Nano-Micro Lett.* **2018**, *10*, 30. [[CrossRef](#)]
- Chen, B.; Wang, T.; Zhao, S.; Tan, J.; Zhao, N.; Jiang, S.P.; Zhang, Q.; Zhou, G.; Cheng, H.M. Efficient Reversible Conversion between MoS₂ and Mo/Na₂S Enabled by Graphene-Supported Single Atom Catalysts. *Adv. Mater.* **2021**, *33*, 2007090. [[CrossRef](#)] [[PubMed](#)]
- Wang, J.; Yue, X.; Xie, Z.; Abudula, A.; Guan, G. MOFs-derived transition metal sulfide composites for advanced sodium-ion batteries. *Energy Storage Mater.* **2021**, *41*, 404–426. [[CrossRef](#)]
- Yin, X.; Ren, Y.; Guo, S.; Sun, B.; Wu, L.; Du, C.; Wang, J.; Yin, G.; Huo, H. Investigating the Origin of the Enhanced Sodium Storage Capacity of Transition Metal Sulfide Anodes in Ether-Based Electrolytes. *Adv. Funct. Mater.* **2022**, *32*, 2110017. [[CrossRef](#)]
- Li, Z.; Feng, W.; Lin, Y.; Liu, X.; Fei, H. Nanostructured ZnCo₂O₄ cathode materials for high-performance lithium-ion batteries. *RSC Adv.* **2016**, *6*, 70632–70637. [[CrossRef](#)]
- Liang, Y.; Lai, W.-H.; Miao, Z.; Chou, S.-L. Nanocomposite Materials for the Sodium-Ion Battery: A Review. *Small* **2018**, *14*, 1702514. [[CrossRef](#)] [[PubMed](#)]
- Su, H.; Yu, H.J. Composite-structure materials for Na-ion batteries. *Small Methods* **2018**, *3*, 1800205. [[CrossRef](#)]
- Long, Y.; Yang, J.; Gao, X.; Xu, X.; Fan, W.; Yang, J.; Hou, S.; Qian, Y. Solid-Solution Anion-Enhanced Electrochemical Performances of Metal Sulfides/Selenides for Sodium-Ion Capacitors: The Case of FeS_{2-x}Se_x. *ACS Appl. Mater. Interfaces* **2018**, *10*, 10945–10954. [[CrossRef](#)] [[PubMed](#)]

25. Li, Y.; Chen, M.; Liu, B.; Zhang, Y.; Liang, X.; Xia, X. Heteroatom Doping: An Effective Way to Boost Sodium Ion Storage. *Adv. Energy Mater.* **2020**, *10*, 2000927. [CrossRef]
26. Zhao, W.; Gao, L.; Ma, X.; Yue, L.; Zhao, D.; Li, Z.; Sun, S.; Luo, Y.; Liu, Q.; Asiri, A.M.; et al. An exquisite branch leaf shaped metal sulfoselenide composite endowing an ultrastable sodium-storage lifespan over 10,000 cycles. *J. Mater. Chem. A* **2022**, *10*, 16962–16975. [CrossRef]
27. Huang, Y.; Wang, Z.; Guan, M.; Wu, F.; Chen, R. Toward Rapid-Charging Sodium-Ion Batteries using Hybrid-Phase Molybdenum Sulfide Selenide-Based Anodes. *Adv. Mater.* **2020**, *32*, 2003534. [CrossRef] [PubMed]
28. He, T.; Zhao, W.; Hu, J.; Deng, C.; Yan, D.; Huang, S. Unveiling the Double-Edged Behavior of Controlled Selenium Substitution in Cobalt Sulfide for Balanced Na-Storage Capacity and Rate Capability. *Adv. Funct. Mater.* **2024**, *34*, 2310256. [CrossRef]
29. Ma, L.; Hu, J.; Deng, C.; Mei, P.; Han, X.; Ba, H.; Li, Z.; Zhang, D.; Huang, S. Promoting the Potassium Storage of 2D Layered Indium Sulfide Through Zinc Incorporation and MXene Coupling. *Adv. Funct. Mater.* **2024**, *34*, 2418733. [CrossRef]
30. Deng, C.J.; Ma, L.Y.; Liu, J.Y.; Han, X.Y.; Zhang, Q.; Jin, J.; Li, Y.; Huang, S.Z. Metal alkoxides: A new type of reversible anode materials for stable and high-rate lithium-ion batteries. *J. Colloid Interf. Sci.* **2024**, *675*, 806–814. [CrossRef] [PubMed]
31. Huang, S.-Z.; Cai, Y.; Jin, J.; Liu, J.; Li, Y.; Yu, Y.; Wang, H.-E.; Chen, L.-H.; Su, B.-L. A new approach to improve the electrochemical performance of $ZnMn_2O_4$ through a charge compensation method. *Nano Energy* **2015**, *12*, 833–844. [CrossRef]
32. Elliott, N. Interatomic distances in FeS_2 , CoS_2 , and NiS_2 . *J. Chem. Phys.* **1960**, *33*, 903–905. [CrossRef]
33. Zhang, Y.; Qiu, Y.; Ji, X.; Ma, T.; Ma, Z.; Hu, P.A. Direct Growth of CNTs@ $CoS_xSe_{2(1-x)}$ on Carbon Cloth for Overall Water Splitting. *ChemSusChem* **2019**, *12*, 3792–3800. [CrossRef]
34. Li, Z.; Bommier, C.; Chong, Z.S.; Jian, Z.; Surta, T.W.; Wang, X.; Xing, Z.; Neufeind, J.C.; Stickle, W.F.; Dolgos, M. Mechanism of Na-Ion Storage in Hard Carbon Anodes Revealed by Heteroatom Doping. *Adv. Energy Mater.* **2017**, *7*, 1602894. [CrossRef]
35. Li, Q.; Jiao, Q.; Yan, Y.; Li, H.; Zhou, W.; Gu, T.; Shen, X.; Lu, C.; Zhao, Y.; Zhang, Y.; et al. Optimized Co-S bonds energy and confinement effect of hollow MXene@ CoS_2 /NC for enhanced sodium storage kinetics and stability. *Chem. Eng. J.* **2022**, *450*, 137922. [CrossRef]
36. Ma, D.; Hu, B.; Wu, W.; Liu, X.; Zai, J.; Shu, C.; Tsega, T.T.; Chen, L.; Qian, X.; Liu, T.L. Highly active nanostructured CoS_2/CoS heterojunction electrocatalysts for aqueous polysulfide/iodide redox flow batteries. *Nat. Commun.* **2019**, *10*, 3367. [CrossRef] [PubMed]
37. Song, H.; Li, T.; He, T.; Wang, Z.; Fang, D.; Wang, Y.; Li, X.L.; Zhang, D.; Hu, J.; Huang, S. Core-Shell Tandem Catalysis Coupled with Interface Engineering for High-Performance Room-Temperature Na-S Batteries. *Chem. Eng. J.* **2022**, *450*, 138115. [CrossRef]
38. Yang, J.; Gao, H.; Men, S.; Shi, Z.; Lin, Z.; Kang, X.; Chen, S. $CoSe_2$ Nanoparticles Encapsulated by N-Doped Carbon Framework Intertwined with Carbon Nanotubes: High-Performance Dual-Role Anode Materials for Both Li- and Na-Ion Batteries. *Adv. Sci.* **2018**, *5*, 1800763. [CrossRef] [PubMed]
39. Chu, C.; Yang, J.; Zhang, Q.; Wang, N.; Niu, F.; Xu, X.; Yang, J.; Fan, W.; Qian, Y. Biphase-Interface Enhanced Sodium Storage and Accelerated Charge Transfer: Flower-Like Anatase/Bronze TiO_2/C as an Advanced Anode Material for Na-Ion Batteries. *ACS Appl. Mater. Inter.* **2017**, *9*, 43648–43656. [CrossRef] [PubMed]
40. Wang, R.; Xue, X.; Lu, W.; Liu, H.; Lai, C.; Xi, K.; Che, Y.; Liu, J.; Guo, S.; Yang, D. Tuning and understanding the phase interface of TiO_2 nanoparticles for more efficient lithium ion storage. *Nanoscale* **2015**, *7*, 12833–12838. [CrossRef]
41. Jin, J.; Zhang, X.; He, T. Self-Assembled CoS_2 Nanocrystal Film as an Efficient Counter Electrode for Dye-Sensitized Solar Cells. *J. Phys. Chem. C* **2014**, *118*, 24877–24883. [CrossRef]
42. Peng, S.; Han, X.; Li, L.; Zhu, Z.; Cheng, F.; Srinivansan, M.; Adams, S.; Ramakrishna, S. Unique Cobalt Sulfide/Reduced Graphene Oxide Composite as an Anode for Sodium-Ion Batteries with Superior Rate Capability and Long Cycling Stability. *Small* **2016**, *12*, 1359–1368. [CrossRef]
43. Huang, P.; Ying, H.; Zhang, S.; Zhang, Z.; Han, W.-Q. Multidimensional synergistic architecture of Ti_3C_2MXene/CoS_2 @N-doped carbon for sodium-ion batteries with ultralong cycle lifespan. *Chem. Eng. J.* **2022**, *429*, 132396. [CrossRef]
44. Ma, Q.; Zhang, L.; Ding, Y.; Shi, X.; Ding, Y.L.; Mujtaba, J.; Li, Z.; Fang, Z. Rational nanostructured $FeSe_2$ wrapped in nitrogen-doped carbon shell for high-rate capability and long cycling sodium-ion storage. *J. Colloid Interf. Sci.* **2022**, *622*, 840–848. [CrossRef] [PubMed]
45. Lu, Z.; Zhai, Y.; Wang, N.; Zhang, Y.; Xue, P.; Guo, M.; Tang, B.; Huang, D.; Wang, W.; Bai, Z.; et al. FeS_2 nanoparticles embedded in N/S co-doped porous carbon fibers as an anode for sodium-ion batteries. *Chem. Eng. J.* **2020**, *380*, 122455. [CrossRef]
46. Chen, D.; Wu, Y.; Huang, Z.; Wang, K.; Zhu, X.; Wang, Z.; Chen, J. Phase transformation controlled $Co_{1-x}S-CoS_2$ heterostructures embedded in S-doped carbon nanofibers for superior Sodium-Ion storage. *Chem. Eng. J.* **2023**, *457*, 141181. [CrossRef]
47. Dong, C.; Guo, L.; Li, H.; Zhang, B.; Gao, X.; Tian, F.; Qian, Y.; Wang, D.; Xu, L. Rational Fabrication of CoS_2/Co_4S_3 @N-Doped Carbon Microspheres as Excellent Cycling Performance Anode for Half/Full Sodium Ion Batteries. *Energy Storage Mater.* **2020**, *25*, 679–686. [CrossRef]
48. Han, F.; Lv, T.; Sun, B.; Tang, W.; Zhang, C.; Li, X. In situ formation of ultrafine CoS_2 nanoparticles uniformly encapsulated in N/S-doped carbon polyhedron for advanced sodium-ion batteries. *RSC Adv.* **2017**, *7*, 30699–30706. [CrossRef]

49. Lin, Y.; Qiu, Z.; Li, D.; Ullah, S.; Hai, Y.; Xin, H.; Liao, W.; Yang, B.; Fan, H.; Xu, J.; et al. NiS₂@CoS₂ nanocrystals encapsulated in N-doped carbon nanocubes for high-performance lithium/sodium-ion batteries. *Energy Storage Mater.* **2018**, *11*, 67–74. [CrossRef]
50. Xie, K.; Li, L.; Deng, X.; Zhou, W.; Shao, Z. A strongly coupled CoS₂/reduced graphene oxide nanostructure as an anode material for efficient sodium-ion batteries. *J. Alloys Compd.* **2017**, *726*, 394–402. [CrossRef]
51. Liu, J.; Xu, Y.G.; Kong, L.B. Cleverly embedded CoS₂/NiS₂ on two-dimensional graphene nanosheets as high-performance anode material for improved sodium ion batteries and sodium ion capacitors. *J. Mater. Sci.-Mater. E.L.* **2020**, *31*, 9946–9959. [CrossRef]
52. He, X.; Bi, L.; Li, Y.; Xu, C.; Lin, D. CoS₂ embedded graphitic structured N-doped carbon spheres interlinked by rGO as anode materials for high-performance sodium-ion batteries. *Electrochim. Acta* **2020**, *332*, 135453. [CrossRef]
53. Zhang, Y.; Wang, N.; Sun, C.; Lu, Z.; Xue, P.; Tang, B.; Bai, Z.C.; Dou, S. 3D spongy CoS₂ nanoparticles/carbon composite as high-performance anode material for lithium/sodium ion batteries. *Chem. Eng. J.* **2018**, *332*, 370–376. [CrossRef]
54. Zhao, Z.; Li, S.; Li, C.; Liu, Z.; Li, D. Hollow CoS₂@C nanocubes for high-performance sodium storage. *Appl. Surf. Sci.* **2020**, *519*, 146268. [CrossRef]
55. Pu, X.; Zhao, D.; Fu, C.; Chen, Z.; Cao, S.; Wang, C.; Cao, Y. Asymmetric Total Synthesis of (-)-Lepadiformine B. *Angew. Chem. Int. Ed.* **2021**, *60*, 21310–21318. [CrossRef]
56. Je, J.; Lim, H.; Jung, H.W.; Kim, S.-O. Ultrafast and Ultrastable Heteroarchitected Porous Nanocube Anode Composed of CuS/FeS₂ Embedded in Nitrogen-Doped Carbon for Use in Sodium-Ion Batteries. *Small* **2022**, *18*, 2105310. [CrossRef] [PubMed]
57. Ma, Y.; Ma, Y.; Bresser, D.; Ji, Y.; Geiger, D.; Kaiser, U.; Streb, C.; Varzi, A.; Passerini, S. A Review on the Recent Advances in Lithium-Sulfur Batteries. *ACS Nano* **2018**, *12*, 7220–7231. [CrossRef] [PubMed]
58. Zhao, W.; Ma, X.; Gao, L.; Wang, X.; Luo, Y.; Wang, Y.; Li, T.; Ying, B.; Zheng, D.; Sun, S.; et al. Hierarchical architecture engineering of branch-leaf-shaped cobalt phosphosulfide quantum dots: Enabling multi-dimensional ion-transport channels for high-efficiency sodium storage. *Adv. Mater.* **2024**, *36*, 2305190. [CrossRef] [PubMed]

Disclaimer/Publisher’s Note: The statements, opinions and data contained in all publications are solely those of the individual author(s) and contributor(s) and not of MDPI and/or the editor(s). MDPI and/or the editor(s) disclaim responsibility for any injury to people or property resulting from any ideas, methods, instructions or products referred to in the content.